CrossMark

Study the dynamic crack path in brittle material under thermal shock loading by phase field modeling

Dongyang Chu · Xiang Li · Zhanli Liu

Abstract A thermal–mechanical coupled phase field fracture model is developed to study the complex dynamic crack propagation path in brittle material under thermal shock loading. By introducing a global continuum phase-field variable to describe the diffusive crack, the coupling between heat transfer, deformation and fracture is conveniently realized. A novel elastic energy density function is proposed to drive the evolution of phase-field variable in a more realistic way. The three-field coupling equations are efficiently solved by adopting a staggered time integration scheme. The coupled phase field fracture model is verified by comparing with three classical examples and is then applied to study the fracture of disk specimens under central thermal shock. The simulations reproduce the three different types of crack paths observed in experiments. It is found that the crack grows through the heating area straightly at lower heating body flux, while branches into two at higher heating body flux loading. The crack branching prefers to occur in the heating area with larger heating radius and prefers to occur outside the heating area with smaller heating radius. Interestingly, the crack branches when propagation speed is at its lowest point, and it always occurs close to the compression region. It is shown that the heterogeneous stress field induced by temperature inhomogeneity may have

a strong influence on the crack branching under the thermal shock loading.

Keywords Dynamic crack propagation · Thermal shock · Phase field modeling · Crack branching

1 Introduction

Thermal shock occurs over a short time scale with a transient temperature variation and leads to significant inhomogeneous volume change and stress distribution in brittle materials. Fracture of material may happen as a grave outcome of thermal shock induced stresses. Due to the combination of inertia effect and complex thermal–mechanical coupling, the mechanism of dynamic thermal shock fracture is quite complicated.

Lots of experiments have been carried out to investigate the thermal shock induced fracture. Some studies focus on understanding the thermal shock stress and induced crack patterns (Jiang et al. 2012; Ronsin et al. 1995; Ronsin and Perrin 1998; Shao et al. 2011), while others pay more attention to evaluating the thermal shock resistance of novel materials (Hongda et al. 2009; Qu et al. 2016; Zhang et al. 2004; Chen et al. 2013). All of these researches show that dynamic failure mechanisms in brittle solids under thermal shock are governed by complex fracture phenomena like crack initiation, crack arrest and multiple crack branching. For example, the periodic parallel cracks and selective arrest appear in quenching tests with glass (Geyer and Nemat-Nasser

D. Chu · X. Li · Z. Liu (✉)
Applied Mechanics Laboratory, Department of
Engineering Mechanics, School of Aerospace, Tsinghua
University, Beijing 100084, China
e-mail: liuzhanli@tsinghua.edu.cn

1982) and ceramics (Jiang et al. 2012; Shao et al. 2011). The instability oscillating crack propagation is discovered under certain thermal shock loading and geometry conditions (Ronsin et al. 1995; Ronsin and Perrin 1998). Different types of crack branching paths are observed when the thermal shock resistance of materials is measured by central heating the disk specimens (Akatsu et al. 2016; Honda et al. 2002; Hongda et al. 2009; Zhang et al. 2004).

Due to the complexity of fracture processes during thermal shock, numerical methods play a crucial role in fracture analyses. The boundary element method (Bahr and Weiss 1988; Tarasovs and Ghassemi 2014), damage-mechanics-based model (Tang et al. 2016) and non-local damage model (Li et al. 2015) have been employed to reproduce the multiple cracking patterns in the quenching test. At the same time, the latter two damage based models can also realize crack initiation. The extended finite element method with nodal enrichment is also used to study the thermal stress evolution and dynamic crack propagation under thermal shock loading (Menouillard and Belytschko 2010; Rokhi and Shariati 2013; Zamani and Eslami 2010). However, these numerical models still have limitations in modeling complex dynamic crack propagation. The damage-mechanics-based model is not directly linked with fracture mechanics theory, and the large spreading damage zones in the simulation results can hardly be regarded as cracks. The boundary element method, non-local method and extended finite element method are associated with fracture mechanics theory. These methods require accurate fracture criterions which are usually difficult to be determined in the case of complex dynamic crack propagation. In addition, both the boundary element method and the extended finite element method need a considerable amount of additional algorithmic structure for tracking the evolution of complex fracture surfaces all the time.

The phase field method for crack propagation modeling links damage and fracture mechanics. This method introduces a global continuous phase-field variable which can be understood as a damage factor to describe the state of material. The governing equation of phase-field variable is derived by minimizing the system free energy which is related to fracture surface energy. The smooth continuum formulations avoid modeling discontinuities as well as tracking complex fracture surfaces and allow to be implemented directly by coupled multi-field finite element solvers. The crack

described by phase field method is diffusive, and the location where the phase-filed variable changes sharply can be regarded as crack surface. By solving the phase-field variable implicitly, complex crack patterns can be modeled without any changes in algorithmic structure. The application of the phase field method to quasi-static crack propagation in brittle solids has been explored by Bourdin et al. (2000), Bourdin (2007), Miehe et al. (2010a, b), Kuhn and Muller (2011), Hesch and Weinberg (2014), Msekh et al. (2015). The dynamic crack propagation in brittle solids has been studied using a phase field method by Karma and Lobkovsky (2004), Henry and Levine (2004), Spatschek et al. (2011), Hofacker and Miehe (2012), Borden et al. (2012), Schlüter et al. (2014). Especially, the phase field model for fracture is very suitable for multi-physics coupling problems because of its smooth continuum character. Using this method, Bourdin et al. (2014) have studied crack initiation, crack arrest and quasi-static crack propagation induced by thermal shock. Corson et al. (2009) have studied quasi-static oscillating crack propagation caused by energy instability under thermal shock. Kuhn and Müller (2009), Miehe et al. (2015) and McAuliffe and Waisman (2015, 2016) build three-field problem models that coupled the deformation with the evolution of temperature and the fracture phase field. In addition, similar multi-field coupling models have appeared in the study of fracture induced by drying of brittle solids (Maurini et al. 2014) and lithium-ion diffusion in the storage particles (Klinsmann et al. 2016; Miehe et al. 2016; Zhang et al. 2016). Most of these studies neglect the inertia effect during the crack propagation which is important under the thermal shock loading. And the influence of the evolving phase-field variable on the change of other material properties like modulus, heat conduction has not been well addressed.

In this paper, we aim at developing a thermal–mechanical coupled phase field fracture model to study the transient heat transfer, dynamic stress evolution and crack propagation in brittle material under thermal shock. The coupling model considers the effect of fracture on the degradation of mechanical and heat transfer property. It will be used to explore the complex crack propagation path influenced by both thermal-shock induced heterogeneous stress field and inertia effect under the thermal shock loading.

This paper is organized as follows. We begin with illustrating the computational model and numerical details in Sect. 2. Then, the model is verified by three

Fig. 1 Deformed configuration of the thermal shock fracture initial boundary value problem. **a** Body with internal discontinuous boundary Γ, which represents a discrete crack. **b** The internal discrete crack is approximated by the phase field d with a diffusive crack topology, and the width of the diffusive crack is controlled by a length parameter l_0
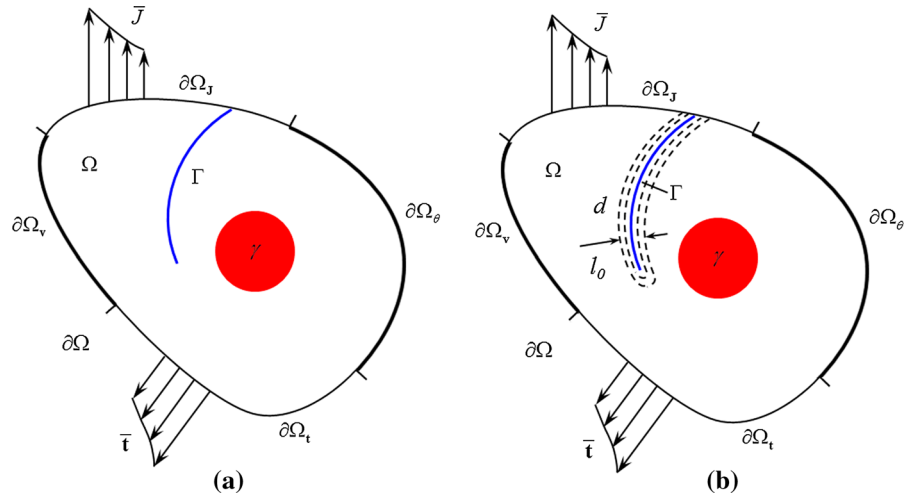
classical numerical examples in Sect. 3, including two dynamic fracture problems of mechanical loading and a quasi-static fracture problem of thermal shock loading. In Sect. 4, the model is employed to investigate the dynamic crack path on disk specimens under central thermal shock. At last, some meaningful results are given in the conclusions.

2 Computational model

In this section the constitutive relations reflecting the coupling among the heat transfer, deformation and fracture are given first. Then, we derive the coupling equations of this multi-physics problem from a global energy balance principle. It is worth mentioning that a modified elastic energy density function that drives the evolution of phase field is used to ensure the simulation results in accordance with the actual situation. At last, the numerical method for solving the coupling equations is introduced.

2.1 Phase field description of fracture

Here, an isotropic elastic body Ω with external boundary $\partial\Omega$ is considered, see Fig. 1a. The latter is divided into $\partial\Omega = \partial\Omega_{\mathbf{J}} \cup \partial\Omega_{\theta}$ and $\partial\Omega = \partial\Omega_{\mathbf{t}} \cup \partial\Omega_{\mathbf{v}}$ for the heat transfer and mechanical deformation problem, respectively. The temperature θ and displacement $\mathbf{u}$ are primary variables which describe heat transfer and deformation of this body, and $\mathbf{v} = \dot{\mathbf{u}}$ is velocity. $\mathbf{J}$ is the heat flux in joules per unit area per unit time,

and $\mathbf{t}$ donates a traction vector applied at $\partial\Omega_{\mathbf{t}}$. The red area in the deformed body Ω represents an internal heat resource γ. Internal heat source and external heat flux change the temperature of the body drastically during the thermal shock, leading to inhomogeneous deformation and fracture of the material. The internal discontinuous boundary Γ in Fig. 1a represents a discrete crack that forms during this process. The discrete crack can be approximated by a diffusive one, which is described by the global continuous fracture phase-field variable d, see Fig 1b. The scalar-valued d with $d = 0$ defining the intact state and $d = 1$ the fully cracked state of the material.

2.2 Effect of fracture phase field on heat transfer and deformation

As stated in Sect. 1, there is a coupling among the heat transfer, deformation and fracture. In this section, this coupling is realized by modifying the elastic stiffness and thermal conductivity as the evolution of phase field fracture variable.

Regarding to deformation field, we confine the model to small deformation. The small strain tensor is

$$\boldsymbol{\varepsilon} = \frac{1}{2}\left(\nabla\mathbf{u} + (\nabla\mathbf{u})^{\mathrm{T}}\right), \tag{1}$$

which can be decomposed into two parts

$$\boldsymbol{\varepsilon} = \boldsymbol{\varepsilon}_e + \boldsymbol{\varepsilon}_\theta \tag{2}$$

where $\boldsymbol{\varepsilon}_e$ and $\boldsymbol{\varepsilon}_\theta$ are elastic and thermal strain tensor respectively. We assume that $\boldsymbol{\varepsilon}_\theta$ is proportional to the temperature

$$\boldsymbol{\varepsilon}_\theta = \alpha\theta\mathbf{I} \tag{3}$$

where α is the linear expansion coefficient of the material, and $\mathbf{I}$ is the identity tensor. According to the linear elastic constitutive model, the stress tensor $\boldsymbol{\sigma}$ is given by

$$\boldsymbol{\sigma} = \mathbf{C} : \boldsymbol{\varepsilon}_e, \quad \mathbf{C} = (1-d)^2\mathbf{C}_0 \tag{4}$$

where $\mathbf{C}_0$ is the inherent isotropic elastic stiffness tensor of the material, and $\mathbf{C}$ is stiffness tensor reduced by phase-field d. The degradation relationship between $\mathbf{C}_0$ and $\mathbf{C}$ given here is consistent with the form given by Miehe et al. (2010a, b).

The heat flux is assumed to be proportional to the gradient of the temperature, given by

$$\mathbf{J} = -k\nabla\theta, \quad k = (1-d)^2k_0 \tag{5}$$

where k is thermal conductivity reduced by phase-field d which can ensure no heat flux at the cracked locations, and k_0 is the inherent thermal conductivity of the material. The degradation function of thermal conductivity has the same format as that of stiffness, because the damage of material should have same reduced effect on all material properties. Thus, there is no heat flux at the crack, and it is reasonable to assume that the thermal behavior in the crack area is adiabatic.

As can be noticed, it is more convenient to deal with the coupling field problem by describing crack using global continuous fracture phase-field variable.

2.3 Coupling equations

The statement of the energy balance principle in the system is written as

$$P^{kin} + P^{\text{int}} = P^{ext} + P^{heat} \tag{6}$$

where P^{kin} and P^{int} denotes the rate of change of kinetic energy and internal energy respectively, P^{ext} the rate of work by the external forces, and P^{heat} the rate of work provided by heat sources and heat flux.

The rate of change of kinetic energy can be expressed as

$$P^{kin}(\mathbf{v}) = \frac{\mathrm{d}}{\mathrm{d}t}\int_\Omega \frac{1}{2}\rho\mathbf{v}\cdot\mathbf{v}\mathrm{d}V. \tag{7}$$

The rate of work by the external forces is given by

$$P^{ext}(\mathbf{v}) = \int_{\partial\Omega_{\mathbf{t}}} \mathbf{t}\cdot\mathbf{v}\,\mathrm{d}S. \tag{8}$$

The rate of work provided by heat sources and heat flux is given by

$$P^{heat} = -\int_{\partial\Omega_\theta} \mathbf{J}\cdot\mathbf{n}\,\mathrm{d}S - \int_{\partial\Omega_{\mathbf{J}}} \bar{J}\,\mathrm{d}S + \int_\Omega \gamma\,\mathrm{d}V, \tag{9}$$

with $\mathbf{n}$ being the outward unit normal vector of the boundary surface, and the superimposed bar indicates the prescribed value on the boundary. In Eq. (9), the first two terms represent the rate of work provided by heat flux from boundary, and the last term is the rate of work provided by heat sources.

For simplicity, we assume that only the heat energy generated by heat sources and external heat flux contributes to the temperature change of the body, and the heat generated by deformation and fracture is negligible. Then, the rate of change of internal energy can be decoupled into three parts,

$$P^{int} = \dot{\Psi}_e + \dot{\Psi}_\Gamma + \dot{\Psi}_\theta \tag{10}$$

where $\dot{\Psi}_e$, $\dot{\Psi}_\Gamma$ and $\dot{\Psi}_\theta$ are the rate of change of elastic energy, crack surface energy and internal energy caused by temperature changes of the body, respectively. The $\dot{\Psi}_\theta$ can be defined as

$$\dot{\Psi}_\theta(\dot{\theta}) = \int_\Omega \rho c\dot{\theta}\,\mathrm{d}V, \tag{11}$$

with ρ and c being the mass density and specific heat of the material respectively. According to classical Griffith theory, the crack surface energy can be calculated by the critical energy release rate G_c integrated over the crack surface, which is expressed as

$$\Psi_\Gamma(\Gamma) = \int_\Gamma G_c\,\mathrm{d}S. \tag{12}$$

As mentioned in Sect. 2.1, the discrete crack Γ is approximated by a diffusive one which is described by the phase-field variable d. Then, the area integral in Eq. (12) can be approximated by a volume integral related to d (Miehe et al. 2010a, b),

$$\Psi_\Gamma \approx \int_\Omega G_c \left[\frac{d^2}{2l_0} + \frac{l_0}{2} |\nabla d|^2 \right] dV \tag{13}$$

where the parameter l_0 controls the width of the diffusive crack. As l_0 approaches zero, a discontinuous function representing a discrete crack is recovered. The elastic energy Ψ_e in Eq. (10) can be expressed as a volume integral of elastic energy density ψ_e in the body Ω,

$$\Psi_e = \int_\Omega \psi_e \, dV. \tag{14}$$

Considering the constitutive relationship given in Eq. (5), the elastic energy density is given by

$$\psi_e(d, \mathbf{u}) = \frac{1}{2} \boldsymbol{\sigma} : \boldsymbol{\varepsilon}_e. \tag{15}$$

Here, for simplicity, the effect of temperature field on elastic energy density is also not considered in this part. Then, the rate of change of ψ_e is written as

$$\dot{\psi}_e(d, \mathbf{u}) = \frac{\partial \psi_e}{\partial \boldsymbol{\varepsilon}_e} : \dot{\boldsymbol{\varepsilon}}_e + \frac{\partial \psi_e}{\partial d} \dot{d}. \tag{16}$$

According to Eq. (5),

$$\dot{\psi}_e = \boldsymbol{\sigma} : \dot{\boldsymbol{\varepsilon}}_e - 2(1-d)\psi_{e0}\dot{d} \tag{17}$$

where

$$\psi_{e0} = \frac{1}{2} \boldsymbol{\varepsilon}_e : \mathbf{C}_0 : \boldsymbol{\varepsilon}_e \tag{18}$$

which can be interpreted as the elastic energy density before reduced by d.

Given the definitions in Eqs. (7)—(11), (13), (14), (17), we substitute them into Eq. (6), leading to

$$\int_\Omega dV \, (\rho c \dot{\theta} + \nabla \cdot \mathbf{J} - \gamma) + \int_\Omega dV \, (\rho \dot{\mathbf{v}} - \nabla \cdot \boldsymbol{\sigma}) \cdot \mathbf{v}$$
$$+ \int_\Omega dV \left[\frac{G_c}{l_0} \left(d - l_0^2 \nabla^2 d \right) - 2(1-d)\psi_{e0} \right] \dot{d}$$

$$+ \int_{\partial \Omega_\mathbf{J}} dS \, (\mathbf{J} \cdot \mathbf{n} - \bar{J}) + \int_{\partial \Omega_\mathbf{t}} dS \, [\boldsymbol{\sigma} \cdot \mathbf{n} - \mathbf{t}] \cdot \mathbf{v}$$
$$+ \int_{\partial \Omega} dS \, (G_c l_0 \nabla d \cdot \mathbf{n}) \dot{d} = 0 \tag{19}$$

where $\dot{\mathbf{v}}$ is the acceleration. Since the energy balance equation must hold for arbitrary values of $\mathbf{v}$ and $\dot{d}$, the strong form of the boundary value problem can be derived:

$$\rho c \dot{\theta} + \nabla \cdot \mathbf{J} = \gamma \quad in \ \partial\Omega,$$
$$\nabla \cdot \boldsymbol{\sigma} = \rho \dot{\mathbf{v}} \quad in \ \Omega,$$
$$\frac{G_c}{l_0}[d - l_0^2 \nabla^2 d] = 2(1-d)\psi_{e0} \quad in \ \Omega,$$
$$\theta = \bar{\theta} \quad on \ \partial\Omega_\theta,$$
$$\mathbf{J} \cdot \mathbf{n} = \bar{J} \quad on \ \partial\Omega_\mathbf{J},$$
$$\mathbf{v} = \bar{\mathbf{v}} \quad on \ \partial\Omega_\mathbf{v},$$
$$\boldsymbol{\sigma} \cdot \mathbf{n} = \bar{\mathbf{t}} \quad on \ \partial\Omega_\mathbf{t},$$
$$\nabla d \cdot \mathbf{n} = 0 \quad on \ \partial\Omega. \tag{20}$$

In addition, we supplement initial conditions in the body as follow:

$$\theta(\mathbf{x}, t) = \theta_0(\mathbf{x}) \quad in \ \Omega,$$
$$\mathbf{u}(\mathbf{x}, t) = \mathbf{u}_0(\mathbf{x}) \quad in \ \Omega,$$
$$\mathbf{v}(\mathbf{x}, t) = \mathbf{v}_0(\mathbf{x}) \quad in \ \Omega. \tag{21}$$

2.4 Modification of the elastic energy density

In the governing equation of phase field, the key term that drives the evolution of d is the elastic energy density ψ_{e0}. However, the expression of ψ_{e0} in Eq. (18) shows a symmetric form of rate-of-deformation tensor, and there is no distinction between tension and compression. This will allow physically unrealistic cracks initiation under compression. To break the symmetry, we modify the elastic energy density as follow:

$$\psi_{e0} = \begin{cases} \psi_{e0} \, , \ tr(\boldsymbol{\varepsilon}_e) \geq 0. \\ \psi_{e0} - \frac{1}{2} K_n tr(\boldsymbol{\varepsilon}_e)^2 \, , \ tr(\boldsymbol{\varepsilon}_e) < 0. \end{cases} \tag{22}$$

Herein, $K_n = \lambda + \frac{2\mu}{n}, n = 2, 3$ is n-dimensional bulk modulus, with λ and μ the Lamé constants. According to Borden et al. (2012), the distinction between tension and compression is particularly important in dynamic problems. Without it, physically unrealistic fracture patterns will be easily created because of the reflection of stress waves in body boundaries.

To avoid crack healing and ensure that the crack growth is irreversible in the case of decreasing ψ_{e0}, the local history field of the maximum energy density (Liu et al. 2016)

$$\mathcal{H}(\mathbf{u}(\mathbf{x}, s)) = \max_{s \in [0,t]} \psi_{e0}(\mathbf{u}(\mathbf{x}, s)) \tag{23}$$

is adopted to replace the ψ_{e0} in Eq. (20). In this manner, the evolution equation for the phase field is

$$\frac{G_c}{l_0}[d - l_0^2 \nabla^2 d] = 2(1 - d)\mathcal{H} \quad in \ \Omega. \tag{24}$$

2.5 Solving the coupling equations

In order to obtain numerical solutions of above initial boundary value problem with a finite element method, we adopt standard procedures to obtain the staggered time integration and implicit iteration formulas of the three field coupling equations in this section.

2.5.1 Finite element discretization

The Galerkin's weak forms of the boundary value problem, Eq. (20), are formulated as follows:

$$\int_{\Omega} \left[\rho c \dot{\theta} \delta \theta \right] dV - \int_{\Omega} [\mathbf{J} \cdot \nabla (\delta \theta)] \, dV$$

$$- \int_{\Omega} [\gamma \delta \theta] \, dV + \int_{\partial \Omega_{\mathbf{J}}} [\bar{J} \delta \theta] \, dA = 0$$

$$\int_{\Omega} [\rho \dot{\mathbf{v}} \cdot \delta \mathbf{u}] \, dV + \int_{\Omega} [\boldsymbol{\sigma} : \delta \boldsymbol{\varepsilon}] \, dV$$

$$- \int_{\partial \Omega_{\mathbf{t}}} [\bar{\mathbf{t}} \cdot \delta \mathbf{u}] \, dV = 0$$

$$\int_{\Omega} \left[\left(\frac{G_c}{l_0} + 2\mathcal{H} \right) (\delta d) \, d \right] dV$$

$$+ \int_{\Omega} [G_c l_0 \nabla d \cdot \nabla (\delta d)] \, dV$$

$$- 2 \int_{\Omega} [\mathcal{H} \delta d] \, dV = 0 \tag{25}$$

where δc, δu and δd are variational test functions. Then, the above weak forms are implicitly solved using finite element method. The 2D linear four-node quadrilateral elements are used to spatially discretize the domain Ω. Therefore, all the volume integrals are actually the area integrals, and all the area integrals are actually the line integrals. Utilizing the Voigt notation, the primary field variables can be discretized by the nodal values θ_I, $\mathbf{u}_I$ and d_I as follows:

$$\theta = \sum_{I=1}^{4} N_I^{\theta} \theta_I, \quad \mathbf{u} = \sum_{I=1}^{4} \mathbf{N}_I^{\mathbf{u}} \mathbf{u}_I, \quad d = \sum_{I=1}^{4} N_I^d d_I \tag{26}$$

where $\mathbf{N}_I^{\mathbf{u}} = \begin{bmatrix} N_I & 0 \\ 0 & N_I \end{bmatrix}$, $N_I^{\theta} = N_I^d = N_I$, and N_I denotes the shape function associated with node I. The corresponding gradients of primary field variables can be expressed as:

$$\nabla \theta = \sum_{I=1}^{4} \mathbf{B}_I^{\theta} \theta_I, \quad \boldsymbol{\varepsilon} = \sum_{I=1}^{4} \mathbf{B}_I^{\mathbf{u}} \mathbf{u}_I, \quad \nabla d = \sum_{I=1}^{4} \mathbf{B}_I^d d_I \tag{27}$$

where $\mathbf{B}_I^{\mathbf{u}} = \begin{bmatrix} N_{I,x} & 0 \\ 0 & N_{I,y} \\ N_{I,y} & N_{I,x} \end{bmatrix}$, $\mathbf{B}_I^{\theta} = \mathbf{B}_I^d = \begin{bmatrix} N_{I,x} \\ N_{I,y} \end{bmatrix}$.

By substituting the space discretization into Eq. (25) and considering the arbitrariness of test functions, the contributions of one element at node I to the global residual of the weak forms can be expressed as

$$\mathbf{R}_I^{\theta} = \int_{\Omega} \left[\rho c \dot{\theta} N_I^{\theta} \right] dV - \int_{\Omega} \left[\mathbf{J} \mathbf{B}_I^{\theta} \right] dV$$

$$- \int_{\Omega} \left[N_I^{\theta} \gamma \right] dV + \int_{\partial \Omega_{\mathbf{J}}} \left[N_I^{\theta} \bar{J} \right] dA$$

$$\mathbf{R}_I^{\mathbf{u}} = \int_{\Omega} \left[\rho \dot{\mathbf{v}} \mathbf{N}_I^{\mathbf{u}} \right] dV + \int_{\Omega} \left[\boldsymbol{\sigma} \mathbf{B}_I^{\mathbf{u}} \right] dV$$

$$- \int_{\partial \Omega_{\mathbf{t}}} \left[\mathbf{N}_I^{\mathbf{u}} \bar{\mathbf{t}} \right] dV$$

$$\mathbf{R}_I^d = \int_{\Omega} \left[\left(\frac{G_c}{l_0} + 2\mathcal{H} \right) N_I^d d \right] dV$$

$$+ \int_{\Omega} \left[G_c l_0 \nabla d \mathbf{B}_I^d \right] dV$$

$$- 2 \int_{\Omega} \left[\mathcal{H} N_I^d \right] dV . \tag{28}$$

Here, all the tensors have been converted to Voigt matrix form.

2.5.2 Time integration and linearization

The time integration of the transient terms in temperature field is approximated by adopting an implicit Backward-Euler method (Bourdin et al. 2010). The updated temperature is

$$\dot{\theta} = \frac{\theta - \theta^n}{\Delta t} \tag{29}$$

with the superscript n representing the value in the previous Δt moment. It is worth mentioning that we regard $n + 1$ moment as the current moment, and the superscript $n + 1$ is not written. An undamped Newmark-β method is employed to update acceleration and velocity (Belytschko et al. 2014):

$$\dot{\mathbf{v}} = \frac{4}{\Delta t} \left[\mathbf{u} - \mathbf{u}^n - \mathbf{v}^n \Delta t - \frac{\Delta t^2}{4} \dot{\mathbf{v}}^n \right]$$
$$\mathbf{v} = \mathbf{v}^n + \frac{\Delta t}{2} \dot{\mathbf{v}}^n + \frac{\Delta t}{2} \dot{\mathbf{v}} . \tag{30}$$

The time integrators used here are unconditionally stable. In Eq. (28), both the stress $\boldsymbol{\sigma}$ and elastic energy density ψ_{e0} used to calculate $\mathcal{H}$ are updated by increments at every time step, with

$$\boldsymbol{\sigma} = \boldsymbol{\sigma}^n + \mathbf{C} : \Delta \boldsymbol{\varepsilon}_e$$
$$\psi_{e0}^n = \psi_{e0}^n + \frac{1}{(1-d)^2} \boldsymbol{\sigma} : \Delta \boldsymbol{\varepsilon}_e. \tag{31}$$

The updated forms of $\boldsymbol{\sigma}$ and ψ_{e0} allow us to conveniently extend the model to simulate the fracture of elastic-plastic material.

Now, the unknown nodal degrees of freedom, including θ, $\mathbf{u}$ and d, need to be solved by making global residual $\mathbf{R}^\theta = 0$, $\mathbf{R}^{\mathbf{u}} = 0$ and $\mathbf{R}^d = 0$ at every time step. Newton's method is utilized to linearize and iteratively solve the nonlinear equations. To improve the iterative convergence and reduce computational complexity, a staggered time integration scheme is adopted. Then, the global residuals in current $n + 1$ moment can be expressed as:

$$\mathbf{R}^\theta(\theta, d \mid \mathbf{u}^n) = 0$$
$$\mathbf{R}^{\mathbf{u}}(\mathbf{u} \mid \theta^n, d^n) = 0.$$
$$\mathbf{R}^d(d \mid \theta^n, \mathbf{u}^n) = 0 \tag{32}$$

The fields behind the vertical bar are taken their values at the last time step and keep constant during solving the current field. The iteration scheme is given as:

$$\mathbf{R}^{\theta(k+1)} = \mathbf{R}^{\theta(k)} - \mathbf{K}^{\theta\theta(k+1)} \Delta\theta^{(k+1)}$$
$$\qquad - \mathbf{K}^{\theta d(k+1)} \Delta d^{(k+1)}$$
$$\mathbf{R}^{\mathbf{u}(k+1)} = \mathbf{R}^{\mathbf{u}(k)} - \mathbf{K}^{\mathbf{u}\mathbf{u}(k+1)} \Delta\mathbf{u}^{(k+1)}$$
$$\mathbf{R}^{d(k+1)} = \mathbf{R}^{d(k)} - \mathbf{K}^{dd(k+1)} \Delta d^{(k+1)} \tag{33}$$

where the index k + 1 indicates the current iteration step, and k means the last iteration step. The corre-

sponding tangent matrices on the element level are

$$\mathbf{K}_{IJ}^{\theta\theta} = \frac{\partial \mathbf{R}_I^\theta}{\partial \theta_J} = \int_\Omega \left[\frac{\rho c}{\Delta t} \left(N_I^\theta \right)^{\mathrm{T}} N_J^\theta \right] \mathrm{d}V$$
$$\qquad + \int_\Omega \left[(1-d)^2 k_0 \left(\mathbf{B}_I^\theta \right)^{\mathrm{T}} \mathbf{B}_J^\theta \right] \mathrm{d}V$$
$$\mathbf{K}_{IJ}^{\theta d} = \frac{\partial \mathbf{R}_I^\theta}{\partial d_J} = \int_\Omega \left[-2(1-d)k_0 \left(\mathbf{B}_I^\theta \right)^{\mathrm{T}} (\nabla\theta) N_J^d \right] \mathrm{d}V$$
$$\mathbf{K}_{IJ}^{\mathbf{u}\mathbf{u}} = \frac{\partial \mathbf{R}_I^{\mathbf{u}}}{\partial \mathbf{u}_J} = \int_\Omega \left[\frac{4\rho}{\Delta t} \left(\mathbf{N}_I^{\mathbf{u}} \right)^{\mathrm{T}} \mathbf{N}_J^{\mathbf{u}} \right] \mathrm{d}V$$
$$\qquad + \int_\Omega \left[(1-d)^2 \left(\mathbf{B}_I^{\mathbf{u}} \right)^{\mathrm{T}} \mathbf{C_0} \mathbf{B}_J^{\mathbf{u}} \right] \mathrm{d}V$$
$$\mathbf{K}_{IJ}^{dd} = \frac{\partial \mathbf{R}_I^d}{\partial d_J} = \int_\Omega \left[G_c l_0 \left(\mathbf{B}_I^d \right)^{\mathrm{T}} \mathbf{B}_J^d \right] \mathrm{d}V$$
$$\qquad + \int_\Omega \left[\left(\frac{G_c}{l_0} + 2\mathcal{H} \right) \left(N_I^d \right)^{\mathrm{T}} N_J^d \right] \mathrm{d}V. \tag{34}$$

As mentioned above, the time integrators adopted here does not need a limitation on time step, and the staggered time integration scheme used to solve the nonlinear equations significantly improves the convergence of iteration. Even so, an appropriate control of the incremental time step should be considered because the staggered time integration scheme will inevitably lead to obvious hysteretic evolution of stress field and phase-field when time step is too large. In particular, the time scale of unstable crack propagation is very short, and time step should be fine enough when simulating the rapid crack growth. Following Borden et al. (2012), during unstable crack propagation, the time step is limited by the propagation time of the Rayleigh wave in one mesh size, i.e. $\Delta t \leq h/v_R$, where h is the mesh size and v_R is the Rayleigh wave speed of material.

3 Verification examples

In this section, two standard examples, the Kalthoff test and dynamic crack branching experiment, are simulated to demonstrate the accuracy of the coupling model in predicting the dynamic crack propagation path. These examples are also used to test the mesh and time step dependency of the coupling model and its corresponding numerical algorithm. After that, the thermal–mechanical coupled phase field fracture model is further validated by simulating the quenching test.
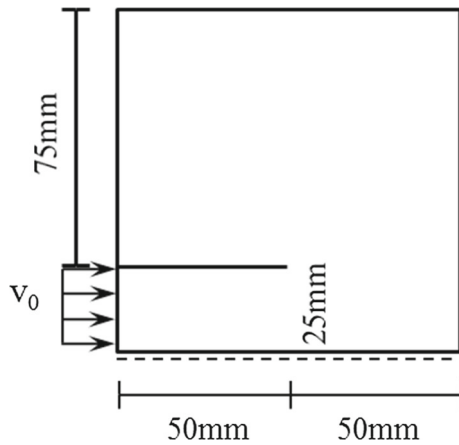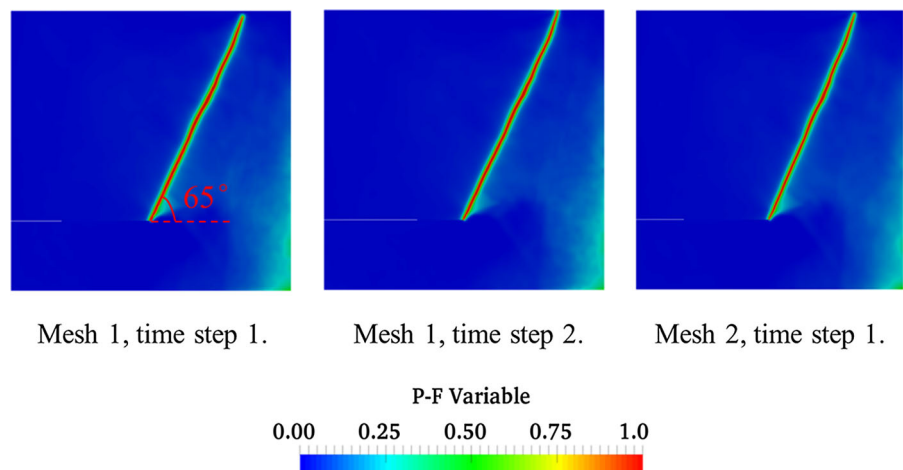
Fig. 2 The geometry and boundary conditions for the Kalthoff test. The *dashed line* represents a symmetric boundary condition

3.1 Kalthoff test

In Kalthoff test (Kalthoff and Winkler 1988; Kalthoff 2000), a symmetrical pre-notched specimen is impacted by a high-speed moving projectile. According to the experiment (Kalthoff 2000), the specimen will crack in a brittle mode when the speed of projectile is in a certain range. To reduce the computational cost, half of specimen is molded considering the symmetry. A schematic of the test is shown in Fig. 2. The velocity of the boundary impacted by the projectile increases linearly to 16.5 m/s in 1 μs, and then keeps constant. The material properties are $\rho = 8000\,\text{kg/m}^3$, $E = 190\,\text{GPa}$, $v = 0.30$ and $G_c = 2.213 \times 10^4\,\text{J/m}^2$. The parameter controlling the diffusive crack width l_0 is set as 3.90×10^{-4} m. In order to test the effect of mesh size and time steps,

two different size of meshes are considered: mesh 1 with $h = 1.95 \times 10^{-4}$ m($h = l_0/2$) and mesh 2 with $h = 0.975 \times 10^{-4}$ m($h = l_0/4$), and the time step is also chosen with different values in case of $\Delta t \leq h/v_R$: time step 1 with $\Delta t = 2.50 \times 10^{-8}$ s and time step 2 with $\Delta t = 1.25 \times 10^{-8}$ s.

The final phase-field variable results at 91 μs for different meshes and time steps are displayed in Fig. 3. It shows that the results have little dependency on mesh and time step. The initial crack propagation angle is about 65°, and the specimen almost breaks completely around 90 μs. These fracture behaviors are consistent with the experiment (Kalthoff 2000) and other published simulation results (Borden et al. 2012; Liu et al. 2016; Song et al. 2007).

3.2 Dynamic crack branching

Dynamic crack branching in a pre-notched glass slab is often simulated to examine the capability of the models to realize crack branching. The geometry and boundary conditions of the test are shown in Fig. 4. A symmetric normal tensile stress $\bar{\mathbf{t}} = 1\,\text{MPa}$ is applied at the top and bottom surfaces, and all other surfaces have no displacement or traction conditions. The similar experiments performed by Ravi-Chandar and Knauss (1984), Sharon and Fineberg (1999) show that the single pre-notched crack will propagate with increasing velocity first and then branches into at least two cracks when the crack tip velocity attains a certain value. The phenomenon is linked with the instability of crack at high propagation speed.
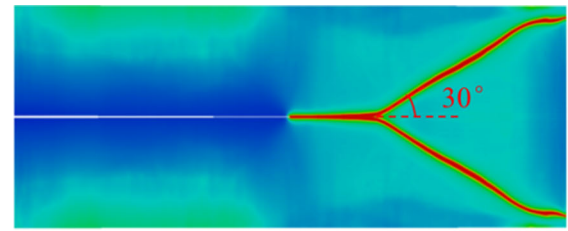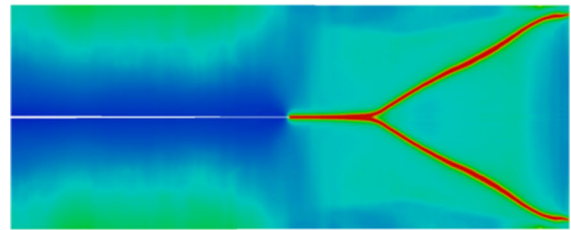
Fig. 3 Contour plot of the phase-field variable at 91 μs for the Kalthoff test with three combinations of mesh and time step

Mesh 1, time step 1.   Mesh 1, time step 2.   Mesh 2, time step 1.

$\bar{t} = 1\text{MPa}$

0.02 m

0.02 m

0.05m

0.1m

Fig. 4 The geometry and boundary conditions for the dynamic crack branching problem

The material properties are $\rho = 2450\,\text{kg/m}^3$, $E = 32\,\text{GPa}$, $\nu = 0.20$ and $G_c = 2700\,\text{J/m}^2$. The corresponding Rayleigh wave speed $v_R = 2125\,\text{m/s}$. The plane strain problem is assumed. The parameter $l_0 = 2.50 \times 10^{-4}$ m and two different square meshes are used: mesh 1 with size $h = 1.25 \times 10^{-4}$ m$(h = l_0/2)$ and mesh 2 with $h = 0.625 \times 10^{-4}$ m$(h = l_0/4)$. Two different time steps are chosen: time step 1 with $\Delta t = 2.50 \times 10^{-8}$ s, time step 2 with $\Delta t = 1.25 \times 10^{-8}$ s, which both meet the basic requirement $\Delta t \leq h/v_R$. The final phase-field variable distributions at $95\,\mu$s obtained from different meshes and time steps are shown in Fig. 5. As we can see, the three crack patterns, especially the branching locations and angles, have just slight difference among each other. The branching angle is around $30°$, which shows little dependency on mesh and time step. Figure 6 illustrates the evolving of crack tip velocity with time. After the crack starts growing around $14\,\mu$s, it accelerates drastically and then branches at a critical velocity of $0.41v_R$ between 29 and $35\,\mu$s. The dashed line in Fig. 7 represents the critical crack branching speed $0.46v_R$ predicted by theoretical analysis of Katzav et al. (2007). Our results, including branching location, angle and critical crack tip velocity, are in good agreement with the same simulations carried by Borden et al. (2012), Schlüter et al. (2014) and theoretical analysis of Katzav et al. (2007).

By simulating Kalthoff test and the dynamic crack branching, we conclude that the thermal–mechanical coupled phase field fracture model can simulate complex crack propagation without any criteria, and the numerical results are reliable when the mesh size and
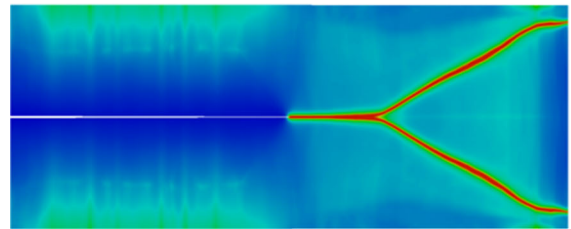

Fig. 5 Contour plot of the phase-field variable at $95\,\mu$s for the dynamic crack branching problem with three combinations of mesh and time step

time step meet $h \leq l_0/2$ and $\Delta t \leq h/v_R$ during unstable crack propagation.

3.3 Quenching test

The quenching test is often used to investigate the thermal shock resistance of various kinds of materials. An experimental study of Shao et al. (2011) on the complex crack patterns induced by thermal shock in ceramics is simulated in this section. In the experiment, the ceramic slabs are heated to different temperature and then dropped by free fall into a water bath. The ceramics with higher temperature before contacting with water
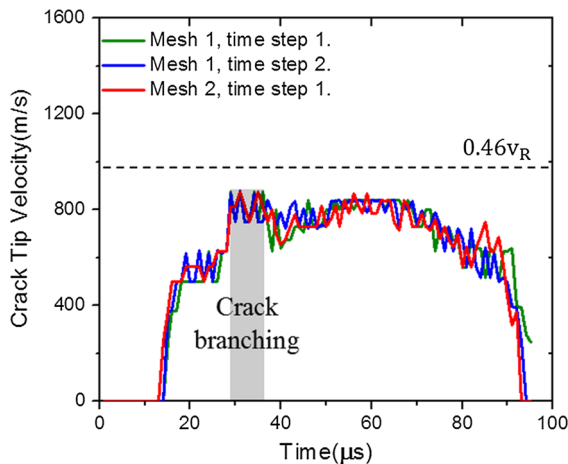
Fig. 6 The evolution of crack tip velocity with time for the dynamic crack branching problem. The *dashed line* represents critical speed $0.46v_R$ predicted by theoretical analysis from Katzav et al. (2007), and crack braches with a critical velocity of $0.41v_R$ between 29 and $35\,\mu s$

shrink more drastically during the quenching, and they exhibit larger quantities of parallel cracks with alternating length. A method based on energy minimization has been used to analyze the periodic array and selective growth of cracks (Jenkins 2005).

According to the experiment, half of a ceramic slab with width of 50 mm and height of 9.8 mm is modeled due to symmetry. The initial temperature of the slab is 680 K, and the temperature of surfaces contacted with water is held constant at $\theta = 300$ K. The flow of water in crack areas is complex, and it is hard to use the degradation of thermal conductivity given in Eq. 5 to reflect a reasonable boundary condition in the crack areas. In addition, previous studies (Bourdin et al. 2014; Jenkins 2005; Tang et al. 2016) also show that the flow of water in crack areas and inertia effect are not key factors leading to these complex crack patterns.

Therefore, the degradation of thermal conductivity and inertia effect are neglected in this section for simplicity. The material properties are $E = 340$ GPa, $v = 0.22$, $G_c = 42.47$ J/m^2 and $\alpha = 8.0 \times 10^{-6}$ K^{-1}. The plane stress is assumed. Thus, the stress field and phase field are both corresponded to global temperature distribution, and the solution of the problem is independent of thermal conductivity. The time t in this section is scaled with the thermal transfer time $\tau = \rho c L^2 / k_0$ where L is the height of the slab. The time step is controlled as two orders of magnitude lower than the crack initiation time. After introducing the phase-field variable to describe cracks, the crack initiation is not only related to the geometry and thermal load of the model but also related to the parameter l_0 (Sicsic et al. 2014). To ensure enough amount of short cracks to be initiated, the l_0 is chosen as 0.092 mm, and the mesh size is set as $h = l_0/4$.

Figure 7 shows the comparison of the final crack patterns between numerical result and experiment. If we neglect the shorter cracks, crack patterns obtained from the numerical tests agree well with the experimental results. During the experiment, shorter cracks probably also nucleate in the slab during first regime (Shao et al. 2011), which cannot be clearly observed due to the limitations of experimental techniques. Our simulation captures the critical features of the problem: a series of periodic parallel short cracks nucleate, followed by selective arrest and growth. The parameter l_0 can ensure sufficient amount of cracks to be initiated to accurately simulate the subsequent process of selective arrest and growth. The cracks can be classified into different hierarchical levels according to the length, and there are three levels both in the numerical and experimental tests. The distribution of temperature and maximum principal stress at $t = 0.004$ are given in Fig. 8. It can be found that the quenching leads to

Fig. 7 The comparison of results between numerical simulation and experiment of a ceramic slab quenching test. The numerical results are evaluated by the distribution of phase-field variable. The distance p and length a of long periodic cracks are marked in the experimental results from Shao et al. (2011)
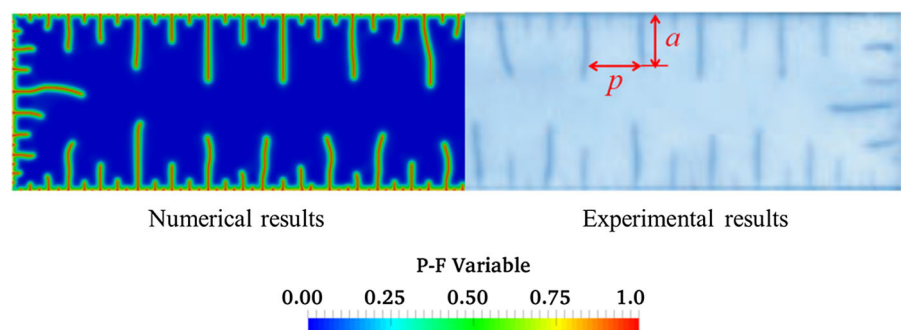
Fig. 8 Contour plot of temperature and maximum principal stress distribution of the model for ceramic quenching test at $t = 0.004$

Temperature (K)
300.　395.　490.　585.　680.

S. Max. Principal (MPa)
-19.2　40.7　81.4　122.　144.
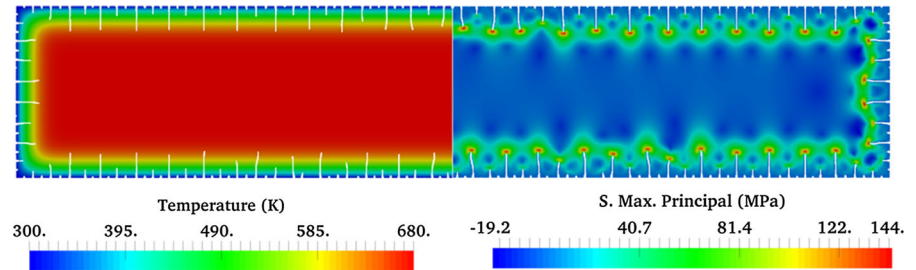
Table 1 The comparison of density and average length of long cracks between numerical and experimental results

	Count n	Average distance p	Average length a
Experiment	12	0.396	0.364
Simulation	11	0.385	0.344

an outer layer with a high temperature gradient and a zone with little temperature change. The crack propagation is stable, and the crack tips evolve along with the boundary of the central high temperature zone. The stress around the arrested crack tips is relatively low.

To evaluate the numerical results quantitatively, the density and average length of long cracks are further compared. Cracks greater than 30% of slab height are defined as long cracks. The density of cracks is quantitated by the frequency count n and average distance p between each other. The comparison is given in Table 1. Here, both a and p are non-dimensionalized by slab height L. The agreement is striking.

The numerical simulation of the problem has shown that our thermal–mechanical coupled phase field fracture model can reproduce the whole process of crack initiation and propagation during thermal shock without any other assumption. The random simulated crack networks are close to real ones in the quenching test, which improves scientific understanding of the formation of thermal shock cracks.

4 Crack path on disk specimens under central thermal shock

4.1 Model description

Another method commonly used to measure the thermal shock resistance of materials is heating the center of disk specimens, and it is easier to quantify than quenching test. Awaji et al. (2002), Honda et al. (2002) and Hongda et al. (2009) have developed standard experiments to test the thermal properties of several materials by infrared radiation heating. In these experiments, a circular area in the center of the disk is heated on the both sides. The limited thermal conductivity of the material and the central sustained heat flux result in the spatial inhomogeneity of temperature distribution, leading to inhomogeneous thermal expansion as well as stress in the disk. When the generated tensile stress reaches to a certain level, the thermal shock fracture occurs. Three types of crack paths are observed in these experiments, as shown in Fig. 9. The first type of crack path, shown in Fig. 9a, is that the crack begins from the pre-notched crack tip, grows through the heating area and reaches the opposite straightly. The second type of crack path, shown in Fig. 9b, grows towards the center of disk in the form of straight line, and then branches into two inside the heating area. The third type of crack path has a similar process as the second one but branches outside the heating area, as shown in Fig. 9c.

To explore the formation mechanism of different crack path, we choose a disk of 30 mm diameter with 2 mm pre-notched crack to study the thermal shock fracture problem. A plane stress problem is assumed. Adiabatic boundary condition is applied around the disk, and the thermal isolation in the crack areas described by Eq. 5 is consistent with the thermal boundary condition. The value of central heat flux is represented by an internal body flux γ (kW/m^3), the radius of heating area is a. The schematic diagram of the model is shown in Fig. 10. According to the literature of experiments (Honda et al. 2002), the material properties of alumina are $E = 380$ GPa, $\nu = 0.25$, $G_c = 26.95$ J/m^2, $\rho = 3900$ kg/m^3, $c = 961.5$ J/(kg K), $k_0 = 21$ W/(m K) and $\alpha = 6.6 \times 10^{-6}$ K^{-1}. The typical Rayleigh wave speed for this material is $v_R = 5.75$ km/s. The phase field
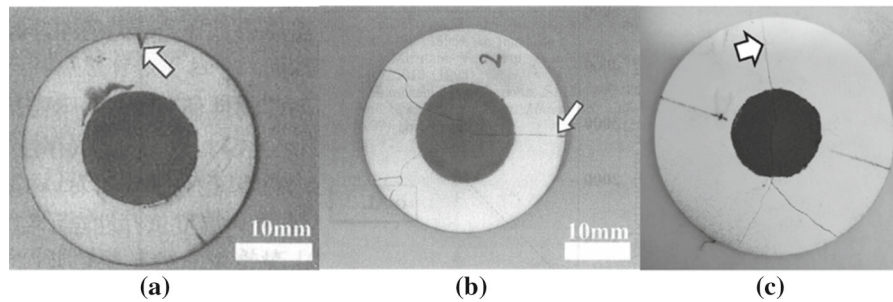
Fig. 9 Three types of crack paths in experiments from Honda et al. (2002) and Hongda et al. (2009). The black zone is the heating area coated with graphite to enhance absorptivity of the infrared rays. **a** Crack grows through the heating area straightly; **b** crack branches into two in the heating area and curves forward; **c** crack branches outside the heating area
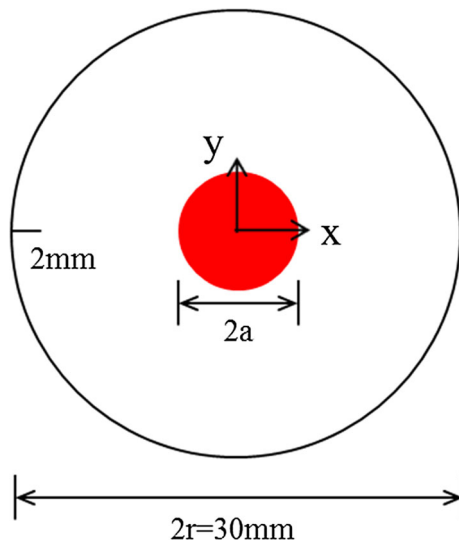
Fig. 10 Geometry and boundary conditions for the thermal shock fracture problem of a disk. The *red area* represents an applied body heat flux. The coordinate origin is set at the center of the disk

parameter is set to $l_0 = 0.1$ mm. The model is meshed uniformly and the mesh size has dimensions $h \leq l_0/2$.

4.2 Crack path affected by heating body flux and radius

In this section, we numerically study the influence of heating body flux and heating radius on the dynamic crack path. The heating radius $a = 2.5, 3.75, 5$ and 7.5 mm, and the heating body flux between 2.5×10^5 and 7.5×10^5 kW/m^3 in step of 2.5×10^5 kW/m^3 are chosen. In all the simulations, about 1000 time steps are guaranteed before the crack begins to grow, and the
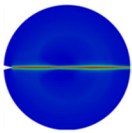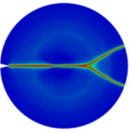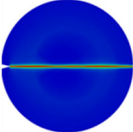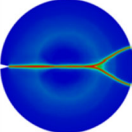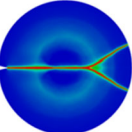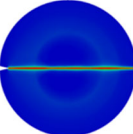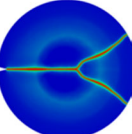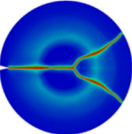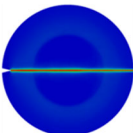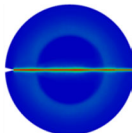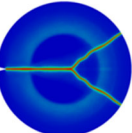
time step is set as $\Delta t = 5 \times 10^{-9}$ s during the unstable crack propagation. According to the experiments, if the pre-notched crack cannot propagate within 10 s, it will be considered that no fracture occurs under this thermal shock load. In addition, once the disk is broken completely, the calculation is stopped. The simulation results for all the cases are listed in Table 2. We can summarize that: the fracture will not occur when the radius and the value of heating body flux are quite small; the first type of crack path appears at lower heating body flux, while the second and the third type of crack path appear at higher body flux; the second type of crack path prefers to occur in the case of larger heating radius, while the third type of crack path prefers to occur in the case of smaller heating radius. For all the simulations in this section, the crack propagation is unstable, and the time scale of crack propagation is much shorter compared with that of heat transfer. The temperature field of the disk almost does not evolve during the crack propagation. Thus, the temperature and stress distribution at the beginning of crack propagation is the crucial factor to lead to different crack patterns. Both the heating radius and body flux can have great effects on the distribution, including amplitude and gradient, of temperature and stress at that moment. Our thermal–mechanical coupled phase field fracture model can numerically reproduce the three types of crack paths observed in the experiments, and the simulation results qualitatively reveal the factors which influence the crack path.

4.3 Discussion on crack branching

The reason for crack branching in a dynamic system is generally considered to be lined with the crack speed

Table 2 Numerical results of the phase-field variable distribution when the disk is broken completely with different heating radius a and heat flux γ for the central thermal shock of a disk

γ(kW/m³) \ a(mm)	2.5×10^5	5×10^5	7.5×10^5
2.5			
3.75			
5			
7.5			

When the disk cannot crack within 10 s, no fracture occurring under this thermal shock load is considered

dependent stress field. As mentioned in Sect. 3.2, the high crack propagation speed leads to the dynamic symmetric branching of a tensile crack. Now, we take the simulation with $a = 5$ mm and $\gamma = 7.5 \times 10^5$ kW/m³ as an example to analyze the details of crack branching. Firstly, the variation of crack tip velocity with the x coordinate is plotted in Fig. 11, where the dashed line represents $0.6v_R$. It can be found that the crack accelerates rapidly to the maximum speed after starting growing, about $0.566v_R$, and then decelerates drastically in the heating area. Interestingly, instead of branching at the highest propagation speed, the crack branches in the loading region with almost the lowest propagation speed. That means the inertia effect is not the only factor to lead to crack branching, because the crack branching induced by inertia effect requires a high crack propagation speed according to the theoretical study of Yoffe (1951) and Katzav et al. (2007).

To further illustrate the mechanism of crack branching, the maximum principal stress distributions around crack tip at different position before crack branching are depicted in Fig. 12. The blue area under compression is roughly the loading area. The gradient stress field is induced by temperature difference of the disk.
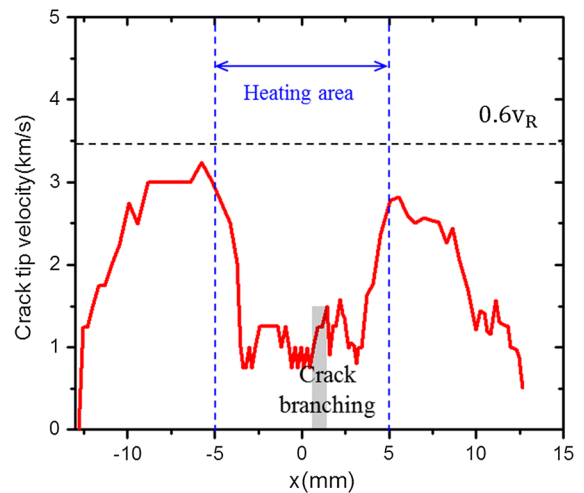

Fig. 11 The evolution of crack tip velocity with x coordinate with $a = 5$ mm and $\gamma = 7.5 \times 10^5$ kW/m³ for the central thermal shock of a disk. The *black dashed line* represents $0.6\,v_R$, and crack branching occurs when crack tip locates at $x = 1.2 \sim 1.4$ mm with low velocity

We can find the high tensile stress gathered at the front of crack tip is gradually distorted with the crack growing though the loading area.
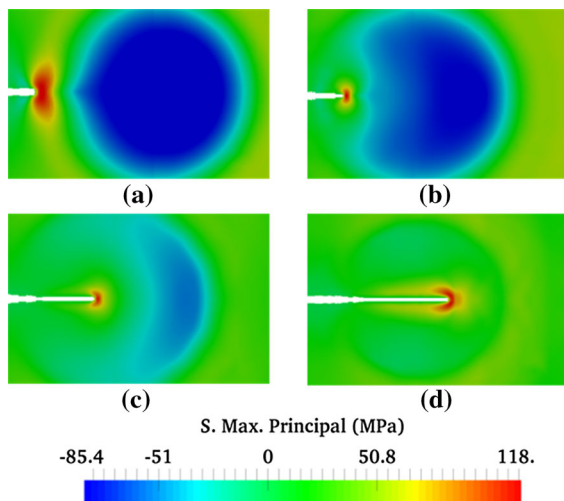
Fig. 12 The maximum principal stress distributions around crack tip for various states of crack propagation before crack branching. **a** Crack tip locates at x = −6 mm. **b** Crack tip locates at x = −3.6 mm. **c** Crack tip locates at x = −0.95 mm. **d** Crack tip locates at x = 1.52 mm
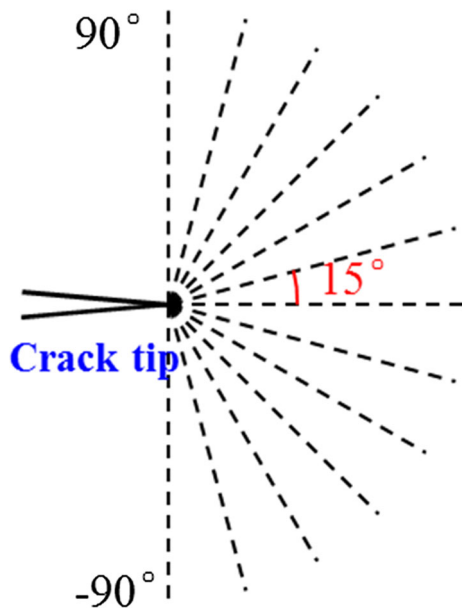
Fig. 13 The schematic of sampling method of the investigation of stress field distribution along different directions around the crack tip

In order to examine the stress distribution around crack tip quantitatively, we output the maximum tensile stress along the direction of every 15° from −90° to 90°. The schematic of sampling around crack tip is illustrated in Fig. 13, and the maximum tensile stress
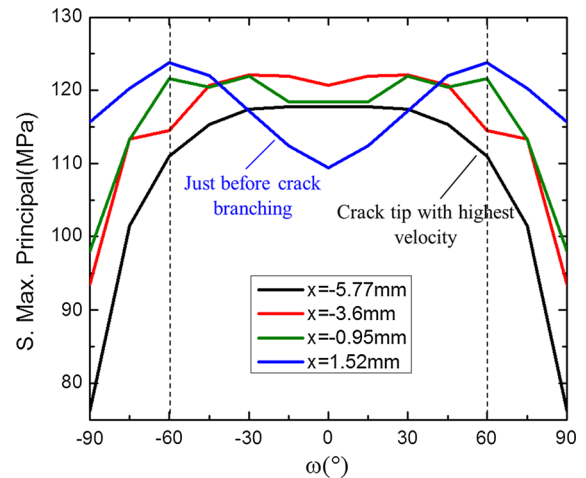
Fig. 14 The polylines of stress maximum around crack tip along different directions when crack tip is in different locations before crack branching

around crack tip along different directions at different time before crack branching is shown in Fig. 14. Obviously, the directions with higher tensile stress values change gradually from 0° to ±60° as the crack approaching the center of compression region. This directional change can be considered as the determinant of crack branching. It also can be found that the direction of higher tensile stress does not deviate when the crack propagates with its highest speed, as shown in Fig. 14. It can be inferred that the crack path deflection in this thermal shock problem is mainly controlled by the gradient stress field induced by the temperature inhomogeneity rather than the crack propagation speed.

5 Conclusion

A thermal–mechanical coupled phase field fracture model is developed in this paper. The phase field fracture model describes crack by introducing a global continuous phase-field variable, and it allows to deal with the coupling field problem more conveniently. A modified elastic energy density which drives the evolution of phase-field variable is used to simulate fracture more realistically. Then, the computational model is solved by a staggered time integration scheme, and it is verified by comparing with several numerical examples. The simulation results demonstrate that the coupling model and numerical method show little dependency on mesh size and time step. The thermal–mechanical

coupled phase field fracture model can simulate complex crack propagation without any criteria and realize crack initiation without any other assumptions.

The thermal–mechanical coupled phase field fracture model is also applied to study the dynamic fracture in disk specimens under thermal shock loading. Our numerical results show three types of crack paths which are in good agreement with experimental results. In addition, the results qualitatively reveal the factors to control different types of crack paths in this problem. The crack grows through the heating area straightly at lower heating body flux loading, while branches into two at higher heating body flux loading. The crack branching prefers to occur in the heating area in the case of larger heating radius and prefers to occur outside the heating area in the case of smaller heating radius. The crack branching at low crack propagation speed is considered to be mainly caused by the heterogeneous stress field induced by temperature inhomogeneity.

References

Akatsu T, Takashima H, Shinoda Y, Wakai F, Wakayama S (2016) Thermal-shock fracture and damage resistance improved by whisker reinforcement in alumina matrix composite. Int J Appl Ceram Technol 13:653–661

Awaji H, Honda S, Yamamoto N, Endo T, Hirosaki N (2002) Thermal shock strength and thermal shock fracture toughness of ceramics. Fract Mech Ceram 13:363–379

Bahr H-A, Weiss H-J (1988) Multiple crack propagation in a strip caused by thermal shock. Theor Appl Fract Mech 10:219–226

Belytschko T, Liu WK, Moran B, Elkhodary KI (2014) Nonlinear finite elements for continua and structures, 2nd edn. Wiley, Chichester

Borden MJ, Verhoosel CV, Scott MA, Hughes TJR, Landis CM (2012) A phase-field description of dynamic brittle fracture. Comput Methods Appl Mech Eng 217–220:77–95

Bourdin B (2007) Numerical implementation of the variational formulation for quasi-static brittle fracture. Interfaces Free Bound 9:411–430

Bourdin B, Francfort GA, Marigo J-J (2000) Numerical experiments in revisited brittle fracture. J Mech Phys Solids 48:797–826

Bourdin B, Larsen CJ, Richardson CL (2010) A time-discrete model for dynamic fracture based on crack regularization. Int J Fract 168:133–143

Bourdin B, Marigo JJ, Maurini C, Sicsic P (2014) Morphogenesis and propagation of complex cracks induced by thermal shocks. Phys Rev Lett 112:014301

Chen HS, Yu X, Guo YZ, Fang DN (2013) Dynamic fracture toughness of piezoelectric ceramics. J Am Ceram Soc 96:2036–2038

Corson F, Adda-Bedia M, Henry H, Katzav E (2009) Thermal fracture as a framework for quasi-static crack propagation. Int J Fract 158:1–14

Geyer JF, Nemat-Nasser S (1982) Experimental investigation of thermally induced interacting cracks in brittle solids. Int J Solids Struct 18:349–356

Henry H, Levine H (2004) Dynamic instabilities of fracture under biaxial strain using a phase field model. Phys Rev Lett 93:105504

Hesch C, Weinberg K (2014) Thermodynamically consistent algorithms for a finite-deformation phase-field approach to fracture. Int J Numer Methods Eng 99:906–924

Hofacker M, Miehe C (2012) Continuum phase field modeling of dynamic fracture: variational principles and staggered FE implementation. Int J Fract 178:113–129

Honda S, Suzuki T, Nishikawa T, Awaji H, Akimune Y, Hirosaki N (2002) Estimation of thermal shock properties for silicon nitride having high thermal conductivity. J Ceram Soc Jpn 110:38–43 **(in Japanese)**

Honda S, Ogihara Y, Kishi T, Hashimoto S, Wamoto YI (2009) Estimation of thermal shock resistance of fine porous alumina by infrared. J Ceram Soc Jpn 117:1208–1215

Jenkins DR (2005) Optimal spacing and penetration of cracks in a shrinking slab. Phys Rev E Stat Nonlinear Soft Matter Phys 71:056117

Jiang CP, Wu XF, Li J, Song F, Shao YF, Xu XH, Yan P (2012) A study of the mechanism of formation and numerical simulations of crack patterns in ceramics subjected to thermal shock. Acta Mater 60:4540–4550

Kalthoff JF (2000) Modes of dynamic shear failure in solids. Int J Fract 101:1–31

Kalthoff J, Winkler S (1988) Failure mode transition at high rates of shear loading. Impact Load Dyn Behav Mater 1:185–195

Karma A, Lobkovsky AE (2004) Unsteady crack motion and branching in a phase-field model of brittle fracture. Phys Rev Lett 92:245510

Katzav E, Adda-Bedia M, Arias R (2007) Theory of dynamic crack branching in brittle materials. Int J Fract 143:245–271

Klinsmann M, Rosato D, Kamlah M, McMeeking RM (2016) Modeling crack growth during Li insertion in storage particles using a fracture phase field approach. J Mech Phys Solids 92:313–344

Kuhn C, Müller R (2009) Phase field simulation of thermomechanical fracture. PAMM 9:191–192

Kuhn C, Muller R (2011) A new finite element technique for a phase field model of brittle fracture. J Theor Appl Mech 44:1115–1133

Li J, Song F, Jiang C (2015) A non-local approach to crack process modeling in ceramic materials subjected to thermal shock. Eng Fract Mech 133:85–98

Liu G, Li Q, Msekh MA, Zuo Z (2016) Abaqus implementation of monolithic and staggered schemes for quasi-static and dynamic fracture phase-field model. Comput Mater Sci 121:35–47

Maurini C, Bourdin B, Gauthier G, Lazarus V (2014) Crack patterns obtained by unidirectional drying of a colloidal suspension in a capillary tube: experiments and numerical simulations using a two-dimensional variational approach. Int J Fract 184:75–91

McAuliffe C, Waisman H (2015) A unified model for metal failure capturing shear banding and fracture. Int J Plast 65:131–151

McAuliffe C, Waisman H (2016) A coupled phase field shear band model for ductile–brittle transition in notched plate impacts. CMAME 305:173–195

Menouillard T, Belytschko T (2010) Analysis and computations of oscillating crack propagation in a heated strip. Int J Fract 167:57–70

Miehe C, Hofacker M, Welschinger F (2010a) A phase field model for rate-independent crack propagation: robust algorithmic implementation based on operator splits. Comput Methods Appl Mech Eng 199:2765–2778

Miehe C, Welschinger F, Hofacker M (2010b) Thermodynamically consistent phase-field models of fracture: variational principles and multi-field FE implementations. Int J Numer Methods Eng 83:1273–1311

Miehe C, Schänzel LM, Ulmer H (2015) Phase field modeling of fracture in multi-physics problems. Part I. Balance of crack surface and failure criteria for brittle crack propagation in thermo-elastic solids. Comput Methods Appl Mech Eng 294:449–485

Miehe C, Dal H, Schänzel LM, Raina A (2016) A phase-field model for chemo-mechanical induced fracture in lithium-ion battery electrode particles. Int J Numer Methods Eng 106:683–711

Msekh MA, Sargado JM, Jamshidian M, Areias PM, Rabczuk T (2015) Abaqus implementation of phase-field model for brittle fracture. Comput Mater Sci 96:472–484

Qu Z, Cheng X, He R, Pei Y, Zhang R, Fang D (2016) Rapid heating thermal shock behavior study of CVD ZnS infrared window material: numerical and experimental study. J Alloys Compd 682:565–570

Ravi-Chandar K, Knauss WG (1984) An experimental investigation into dynamic fracture: III. On steady-state crack propagation and crack branching. Int J Fract 26:141–154

Rokhi MM, Shariati M (2013) Implementation of the extended finite element method for coupled dynamic thermoelastic fracture of a functionally graded cracked layer. J Braz Soc Mech Sci Eng 35:69–81

Ronsin O, Perrin B (1998) Dynamics of quasistatic directional crack growth. Phys Rev E 58:7878–7886

Ronsin O, Heslot F, Perrin B (1995) Experimental study of quasistatic brittle crack propagation. Phys Rev Lett 75:2352–2355

Schlüter A, Willenbücher A, Kuhn C, Müller R (2014) Phase field approximation of dynamic brittle fracture. Comput Mech 54:1141–1161

Shao Y, Zhang Y, Xu X, Zhou Z, Li W, Liu B, Jin ZH (2011) Effect of crack pattern on the residual strength of ceramics after quenching. J Am Ceram Soc 94:2804–2807

Sharon E, Fineberg J (1999) Confirming the continuum theory of dynamic brittle fracture for fast cracks. Nature 397:333–335

Sicsic P, Marigo J-J, Maurini C (2014) Initiation of a periodic array of cracks in the thermal shock problem: a gradient damage modeling. J Mech Phys Solids 63:256–284

Song JH, Wang H, Belytschko T (2007) A comparative study on finite element methods for dynamic fracture. Comput Mech 42:239–250

Spatschek R, Brener E, Karma A (2011) Phase field modeling of crack propagation. Philos Mag 91:75–95

Tang SB, Zhang H, Tang CA, Liu HY (2016) Numerical model for the cracking behavior of heterogeneous brittle solids subjected to thermal shock. Int J Solids Struct 80:520–531

Tarasovs S, Ghassemi A (2014) Self-similarity and scaling of thermal shock fractures. Phys Rev E Stat Nonlinear Soft Matter Phys 90:012403

Yoffe EH (1951) LXXV. The moving griffith crack. London Edinb Dublin Philos Mag J Sci 42(330):739–750

Zamani A, Eslami MR (2010) Implementation of the extended finite element method for dynamic thermoelastic fracture initiation. Int J Solids Struct 47:1392–1404

Zhang XH, Han JC, He XD, Yan C, Wang BL, Xu Q (2004) Ablation-resistance of combustion synthesized TiB$_2$-Cu cermet. J Am Ceram Soc 88:89–94

Zhang X, Krischok A, Linder C (2016) A variational framework to model diffusion induced large plastic deformation and phase field fracture during initial two-phase lithiation of silicon electrodes. Comput Methods Appl Mech Eng 312:51–77